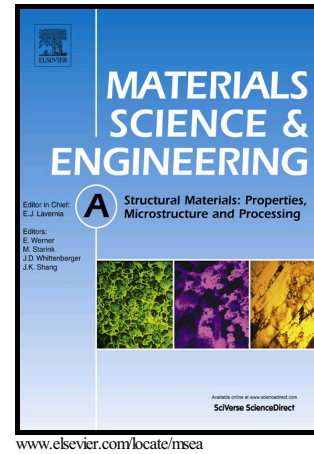


# Author's Accepted Manuscript

Effect of Mo addition on the microstructure and hardness of ultrafine-grained Ni alloys processed by a combination of cryorolling and high-pressure torsion

Garima Kapoor, Yi Huang, V. Subramanya Sarma, Terence G. Langdon, Jenő Gubicza



PII: S0921-5093(17)30138-7  
DOI: <http://dx.doi.org/10.1016/j.msea.2017.01.104>  
Reference: MSA34666

To appear in: *Materials Science & Engineering A*

Received date: 19 December 2016  
Revised date: 29 January 2017  
Accepted date: 30 January 2017

Cite this article as: Garima Kapoor, Yi Huang, V. Subramanya Sarma, Terence G. Langdon and Jenő Gubicza, Effect of Mo addition on the microstructure and hardness of ultrafine-grained Ni alloys processed by a combination of cryorolling and high-pressure torsion, *Materials Science & Engineering A* <http://dx.doi.org/10.1016/j.msea.2017.01.104>

This is a PDF file of an unedited manuscript that has been accepted for publication. As a service to our customers we are providing this early version of the manuscript. The manuscript will undergo copyediting, typesetting, and a review of the resulting galley proof before it is published in its final citable form. Please note that during the production process errors may be discovered which could affect the content, and all legal disclaimers that apply to the journal pertain

**Effect of Mo addition on the microstructure and hardness of ultrafine-grained Ni alloys  
processed by a combination of cryorolling and high-pressure torsion**

Garima Kapoor<sup>a</sup>, Yi Huang<sup>b</sup>, V. Subramanya Sarma<sup>c</sup>, Terence G. Langdon<sup>b</sup>, Jenő Gubicza<sup>a\*</sup>

<sup>a</sup>Department of Materials Physics, Eötvös Loránd University, P.O.B.32, Budapest, H-1518, Hungary

<sup>b</sup>Materials Research Group, Faculty of Engineering and the Environment, University of Southampton, Southampton SO171BJ, UK

<sup>c</sup>Department of Metallurgical and Materials Engineering, Indian Institute of Technology Madras, Chennai 600036, India

\*Corresponding author: Tel: +36-1-372-2876, Fax: +36-1-372-2811,  
e-mail: jeno.gubicza@ttk.elte.hu

**Abstract**

An investigation was conducted to examine the effect of molybdenum (Mo) content on the grain size, lattice defect structure and hardness of nickel (Ni) processed by severe plastic deformation (SPD). The SPD processing was applied to Ni samples with low (~0.3 at.%) and high (~5 at.%) Mo concentrations by a consecutive application of cryorolling and high-pressure torsion (HPT). The grain size and the dislocation density were determined by scanning electron microscopy and X-ray line profile analysis, respectively. In addition, the hardness values in the centers, half-radius and peripheries of the HPT-processed disks was determined after ½, 5 and 20 turns. The results show the higher Mo content yields a dislocation density about two times larger and a grain size about 30% smaller. The smallest value of the grain size was ~125 nm and the highest measured dislocation density was  $\sim 60 \times 10^{14} \text{ m}^{-2}$  for Ni-5% Mo. For the higher Mo concentration, the dislocation arrangement parameter was larger indicating a less clustered dislocation structure due to the hindering effect of Mo on the rearrangement of dislocations into low energy configurations. The results show there is a good correlation between the dislocation density and the yield strength using the Taylor equation. The  $\alpha$  parameter in this equation is slightly lower for the higher Mo concentration in accordance with the less clustered dislocation structure.

**Keywords:** cryorolling; hardness; high-pressure torsion; microstructure; Ni-Mo alloys

## 1. Introduction

Porosity and contamination-free, bulk ultrafine-grained (UFG) or nanocrystalline materials can be produced with improved mechanical performance using severe plastic deformation (SPD) techniques [1-3]. One of the most effective SPD methods for grain refinement and strength increment is high-pressure torsion (HPT) [4-8]. Except at the center of the HPT-processed disk, the large shear strain and the high applied pressure lead to a very high dislocation density which makes a significant contribution to the large hardness of the samples deformed by this technique [9]. Nevertheless, experiments show that a combination of HPT with other SPD and non-SPD processing routes (such as rolling) gives the potential for achieving a greater grain refinement in bulk metallic materials [10-12]. Among non-SPD techniques, cryorolling is very effective in achieving a small grain size because the extremely low temperature (usually liquid nitrogen temperature is applied) suppresses any dynamic recovery of the dislocation structure and the occurrence of grain growth during deformation [13]. Therefore, a combination of cryorolling and subsequent HPT at room temperature (RT) appears to be a promising SPD method for the production of metals and alloys with UFG or nanocrystalline microstructures.

It is known that the grain refinement and the increase in the dislocation density during SPD processing may be further enhanced through the addition of alloying elements to metallic materials [9,14]. The pinning effect of solute atoms and precipitates on dislocations and grain boundaries in alloys impedes the dislocation annihilation and grain coarsening, thereby leading to an improved mechanical strength in the SPD-processed materials. In the past two decades, numerous investigations were carried to study the microstructure and the mechanical properties of various SPD processed alloys, such as Al-Mg, Al-Zn-Mg, Cu-Zn, Cu-Al, Cu-Cr, Cu-Zr etc. [14-23]. However, no research was conducted to date to examine the effect of Mo solute atoms on the microstructure of UFG Ni processed by SPD, although Ni-Mo alloys have

important practical applications. For example, these alloys are used as catalysts in hydrogen production [24-26] and as substrate material for superconducting coatings [27]. It was shown that Ni-Mo alloys exhibit high activity and long-term stability as the hydrogen evolution reaction under alkaline conditions occurs either in the form of a catalyst coating [24] or as unsupported nanopowder [25,26]. Nanocrystalline electrodeposited Ni-Mo thin films are potentially applicable as novel catalytic materials with ferromagnetism [28]. The Ni-Mo substrates for superconducting coatings are produced by severe cryorolling and subsequent annealing resulting in an extremely sharp cube texture which is required for epitaxial coatings. These Ni-Mo alloys also exhibit high hardness, wear, thermal and corrosion resistance, and therefore they are readily useful as hard coating materials [29].

The objective of this study was to investigate the impact of varying Mo contents on the microstructure and hardness of a UFG Ni alloy processed by SPD. For this purpose, two alloys with low (~0.3 at.%) and high (~5 at.%) Mo concentrations were processed by the consecutive application of cryorolling and HPT at RT. The evolution of microstructure, including grain size and dislocation density, with increasing SPD straining was characterized using different experimental methods. In addition, the hardness values were investigated both for the cryorolled samples and for disks processed for ½, 5 and 20 turns of HPT. The yield strength was determined as one third of the hardness and correlated to the dislocation density.

## **2. Experimental materials and procedures**

### *2.1. Processing of UFG Ni-Mo alloys*

Ni alloys with low (~0.3 at.%) and high (~5 at.%) Mo contents were prepared by induction melting and casting into a Cu-mould. The as-cast ingots, having diameters of ~32 mm, were hot rolled at 1100°C to a thickness of ~13 mm. The hot rolled samples were subjected to a two-step combined SPD process. In the first step, small strips were cut from the hot rolled materials and cryorolled at liquid nitrogen temperature (LNT). During cryorolling, the

thickness decreased from ~13 mm to ~3 mm in multiple passes with a thickness reduction of ~5% per pass. After each cryorolling pass, the strips were cooled again to LNT. From the plates obtained after cryorolling, discs were prepared with diameters of 10 mm and thicknesses of 1 mm. These samples were then processed by HPT technique under quasi-constrained conditions [30] with an applied pressure of 6.0 GPa and rotating speed of 1 rpm at RT for ½, 5 and 20 turns. The chemical compositions of the HPT-processed Ni alloys were determined by energy dispersive spectroscopy (EDS) in a scanning electron microscope (SEM) and the results are listed in Table 1. The Mo concentrations in the alloys with low and high Mo contents were 0.28 and 5.04 at.%, respectively. Hereafter, the materials with low and high Mo concentrations are designated Low-Mo and High-Mo, respectively. It is noted that, in addition to Mo, other elements such as Al, Fe and Si were also detected in the samples. Nevertheless, the most significant difference between the chemical compositions of the two samples was the much higher Mo content in the material labelled High-Mo.

## 2.2. Microstructure from EBSD

The microstructures of the cryorolled and the HPT-processed Ni alloys were characterized by electron backscatter diffraction (EBSD) using an FEI Quanta 3D SEM. It is noted that the same device was used for the EDS analysis presented above. For the HPT-processed samples, the EBSD investigations were carried out at the center, half-radius and periphery of the disks. Before EBSD, the surfaces of the samples were first mechanically polished with 600, 1200, 2500 and 4000 grit SiC abrasive papers and then the surface treatment was continued by polishing with a colloidal silica suspension (OP-S) having a particle size of 1 micrometer. Finally, electropolishing of the surfaces was conducted at 28 V and 1A using an electrolyte with a composition of 70% ethanol, 20% glycerine and 10% perchloric acid (in vol %). The step size in the EBSD study was ~30 nm and the EBSD images were evaluated using the Orientation Imaging Microscopy (OIM) software. The average grain sizes and the fractions of

the low and high-angle grain boundaries (LAGBs and HAGBs) were determined from the EBSD images by investigating the misorientations in the SPD processed microstructures [31,32]. The grains were considered as the regions in the EBSD images bounded by high-angle grain boundaries (HAGBs) having misorientations higher than  $15^\circ$ . The number-averaged grain size values are also reported in this study.

### 2.3. Characterization of microstructure by X-ray diffraction

The average lattice parameter values for the Ni alloys were determined by X-ray diffraction (XRD) using a Philips Xpert  $\Theta$ - $2\Theta$  powder diffractometer operating at 40 kV and 30 mA with  $\text{CuK}\alpha$  radiation (wavelength:  $\lambda = 0.15418$  nm). The measured XRD patterns indicated that all samples had face-centered cubic (fcc) structure. The average lattice parameter was determined from the diffraction peak positions using the Nelson–Riley method [33].

The microstructures of the SPD-processed Ni alloys were studied by X-ray line profile analysis (XLPA). For the HPT-processed samples, the XLPA investigations were carried out at the center, half-radius and periphery of the disks. The XRD patterns were measured by a high-resolution diffractometer (Rigaku) with  $\text{CuK}\alpha_1$  radiation (wavelength:  $\lambda = 0.15406$  nm). The Debye–Scherrer diffraction rings were detected by two dimensional imaging plates and the line profiles were determined as the intensity distributions perpendicular to the rings obtained by integrating the two dimensional intensity distributions along the rings. The evaluation of the patterns was carried out by the Convolutional Multiple Whole Profile (CMWP) fitting method [34]. In this procedure, the experimental diffraction pattern is fitted by the sum of a background spline and the convolution of the instrumental pattern and the theoretical line profiles related to crystallite size, dislocations and planar faults. The instrumental broadening was negligible, compared to the physical peak broadening due to the UFG microstructure of the samples and therefore an instrumental correction was not necessary. The theoretical line profile functions used in this fitting procedure were based on a

model of the microstructure where the crystallites have spherical shape and a log-normal size distribution. The following parameters of the microstructure were determined by the CMWP fitting procedure: the area-weighted mean crystallite size ( $\langle x \rangle_{\text{area}}$ ), the twin fault probability ( $\beta$ ), the average dislocation density ( $\rho$ ) and the dislocation arrangement parameter  $M$ . The twin fault probability in fcc materials is defined as the relative fraction of twin boundaries among the  $\{111\}$  lattice planes. The value of the parameter  $M$  reflects the arrangement of the dislocations. Thus, a smaller value of  $M$  relates to a more shielded strain field of the dislocations and the arrangement of dislocations into low energy configurations, such as LAGBs or dipoles, yields a consequent decrease in  $M$ . The area-weighted mean crystallite size ( $\langle x \rangle_{\text{area}}$ ) was calculated as  $\langle x \rangle_{\text{area}} = m \cdot \exp(2.5 \sigma^2)$ , where  $m$  is the median and  $\sigma^2$  is the log-normal variance of the crystallite size distribution.

#### 2.4. Microhardness testing

The microhardness of the SPD-processed samples was determined using a Zwick Roell ZH $\mu$  hardness tester with a Vickers indenter, an applied load of 500 g and a dwell time of 10 s. Due to the anticipated gradient in the microstructure along the radius of the HPT disks, the hardness was measured at the center, half-radius and periphery of the HPT-processed samples.

### 3. Experimental results

#### 3.1. Lattice parameter of the SPD-processed Ni alloys

The average lattice parameters for the cryorolled and the HPT processed alloys were determined by XRD. The values of the lattice parameter for both the cryorolled and the HPT-processed specimens were  $0.3527 \pm 0.0002$  and  $0.3549 \pm 0.0002$  nm for the Low-Mo and High-Mo alloys, respectively. These values deviate from the lattice constant of pure Ni (0.3524 nm) because of the considerable alloying elements that are concentrated in these

alloys (see Table 1). Thus, it was reported that the addition of Mo, Al and Fe to Ni increases the lattice parameter while alloying with Si leads to a decrease of the lattice constant [35].

In the present alloys, the largest effects on the lattice parameter are caused by the additions of Mo and Al whereas the effects of Fe and Si approximately compensate each other. Therefore, the lattice parameter of the present alloys may be estimated as:

$$a = 0.3524 + 0.0478 \cdot x_{MO} + 0.0179 \cdot x_{Al} , \quad (1)$$

where  $x_{Mo}$  and  $x_{Al}$  are the mole fractions of Mo and Al, respectively. Using the concentration values in Table 1, eq. (1) gives estimates of 0.3527 and 0.3550 nm for the lattice parameters of the Low-Mo and High-Mo alloys, respectively, and these values agree with the measured lattice constants within experimental error. This agreement between the measured and the calculated lattice parameters indicates that all of the alloying elements are in solid solution. Thus, as the equilibrium solubility limit of Mo in Ni is only about 0.6 at.%, the High-Mo alloy is a supersaturated solid solution.

### 3.2. Characterization of the microstructure for cryorolled and HPT-processed Ni alloys by EBSD

Fig. 1 shows EBSD images obtained from the cryorolled Low-Mo (a and b) and High-Mo (c and d) alloys. The HAGBs are indicated by black lines in the images. For each alloy two images are shown with low (Figs. 1a and c) and high magnifications (Figs. 1b and d) due to the complex nature of the microstructures. Indeed, the low magnification images in Figs. 1a and c reveal that there are large grains with the dimensions of several tens of microns while in other regions the grain size is only a few microns. The high magnification images in Figs. 1b and d show that there are grains which are even smaller than one micron in the Low-Mo and High-Mo alloys, respectively. The average grain sizes for the cryorolled Low-Mo and High-Mo samples were  $\sim 4.1$  and  $\sim 3.8$   $\mu\text{m}$ , respectively. The microstructure evolutions in the Low-Mo and High-Mo alloys during HPT are illustrated by the EBSD images in Figs. 2 and 3

where these images correspond to the centers (on left) and the peripheries (on right) for the lowest and the highest numbers of HPT turns corresponding to (a,b) 1/2 and (c,d) 20 revolutions, respectively. For better visibility of the grains in the centers of the disks processed by 1/2 turn, the HAGBs are indicated by black lines. The grain size values determined for these two alloys in the disk center, half-radius and periphery positions for 1/2, 5 and 20 HPT turns are plotted in Fig. 4(a) and (b) for the Low-Mo and High-Mo alloys, respectively.

For the Low-Mo alloy, a significant grain refinement was observed in the center of the disk processed by 1/2 turn since the grain size decreased to  $\sim 1.9 \mu\text{m}$ , and at the periphery the grain size was even smaller at  $\sim 205 \text{ nm}$  due to the higher applied shear strain. For 20 turns, the microstructure became more homogeneous along the disk radius and the grain sizes in the center and the periphery were  $\sim 225$  and  $\sim 180 \text{ nm}$ , respectively. For the High-Mo alloy, there were much smaller grain sizes in the center ( $\sim 930 \text{ nm}$ ) and at the periphery ( $\sim 135 \text{ nm}$ ) after 1/2 turn than for the Low-Mo alloy because of the higher Mo content. With increasing numbers of turns to 20 for the High-Mo alloy, the grain sizes in the center and periphery were further refined to  $\sim 170$  and  $\sim 125 \text{ nm}$ , respectively. These values are considerably smaller than the grain sizes obtained for the Low-Mo alloy but for both compositions the grain size decreases with both increasing distance from the disk center and increasing numbers of turns. It is apparent from these measurements that the higher Mo content yielded  $\sim 30\%$  smaller saturation grain size and for this alloy the grain size at the periphery saturated after approximately 1/2 turn of HPT.

The fraction of HAGBs was also determined from the EBSD images for the cryorolled and HPT-processed Low-Mo and High-Mo specimens. Fig. 5 shows the HAGB fraction for the center, half-radius and periphery of the disks processed for 1/2, 5 and 20 turns. After cryorolling, the fractions of HAGBs were only  $\sim 11$  and  $\sim 16\%$ , respectively. HPT processing

produced a significant increase in the HAGB fraction for both compositions. With increasing distance from the disk center and the number of turns, the fraction of HAGBs was further increased. A maximum HAGB fraction of about ~70% was achieved at the periphery even after ½ turn. For 20 turns of HPT, saturations were achieved in both alloys at the half-radius positions. Finally, it is important to note there are no significant differences between the saturation values of the HAGB fractions in the Low-Mo and High-Mo alloys.

### *3.3. Influence of Mo content on density and arrangement of dislocations as determined by XPLA*

The dislocation densities and the dislocation arrangement parameters for the cryorolled and HPT-processed Low-Mo and High-Mo alloys were determined by XLPA. Fig. 6 illustrates the CMWP fitting for the High-Mo alloy in the center of the disk processed by 20 HPT turns. The open circles and the solid line correspond to the measured and fitted intensity profiles, respectively. In the cryorolled Low-Mo and High-Mo alloys, the dislocation density values were  $\sim 15 \times 10^{14} \text{ m}^{-2}$  and  $\sim 35 \times 10^{14} \text{ m}^{-2}$ , respectively. The higher dislocation density in the alloy containing the larger Mo content is due to the stronger effect of the larger Mo solute atoms in impeding dislocation annihilation during cryorolling.

Fig. 7 shows that HPT processing led to a further enhancement in the dislocation density. For the Low-Mo alloy, an early saturation of the dislocation density was observed and its value changes only slightly either along the disk radius or as a function of the number of HPT turns. The maximum dislocation density in the Low-Mo alloy achieved by the subsequent application of cryorolling and HPT was  $\sim 30 \times 10^{14} \text{ m}^{-2}$ . For the High-Mo alloy processed by ½ turn, the dislocation density was significantly enhanced with increasing distance from the center and reached a value of  $\sim 60 \times 10^{14} \text{ m}^{-2}$  at the disk periphery. This value can be regarded as the saturation value of the dislocation density for the HPT-processed

High-Mo alloy since after 5 and 20 turns the dislocation density did not exceed this value but it became more homogeneous along the disk radius. Thus, it is concluded that the higher Mo content yielded a larger dislocation density by a factor of two times in the alloys processed by the subsequent application of cryorolling and HPT and this is attributed to the pinning effect of the solute Mo atoms on dislocations. The use of XLPA permits a determination of the dislocation arrangement parameter,  $M$ , and after cryorolling and HPT the values of  $M$  were in the ranges of  $\sim 2.3 \pm 0.6$  and  $\sim 5.0 \pm 0.5$  for the Low-Mo and High-Mo alloys, respectively. The higher  $M$  value for High-Mo alloy is also explained by the pinning effect of the solute Mo atoms on the dislocations which impedes their re-arrangement into low energy configurations.

In addition to the density and the arrangement parameter of dislocations, the crystallite size was also determined from an analysis of the X-ray diffraction peak profiles. The average crystallite sizes were  $\sim 40$  and  $\sim 30$  nm for the Low-Mo and High-Mo alloys processed by the consecutive application of cryorolling and HPT, respectively. There were no major changes in the crystallite size with increasing distance from the center or with the number of turns. Both the values of the crystallite sizes determined by XLPA and their evolutions with increasing strain were different from the grain sizes obtained by EBSD. This difference is due to the hierarchical microstructure in SPD-processed metals where the grains are subdivided into subgrains and/or dislocation cells which scatter X-rays incoherently [36]. Therefore, XLPA measures the size of the subgrains and cells as the crystallite size, also defined as the coherently-scattered domain size, and this is smaller than the grain size in SPD-processed materials. The twin fault probability in both Low-Mo and High-Mo alloys processed by SPD was under the detection limit of the present XLPA method (0.1%), indicating that twinning has no significant role in cryorolling and HPT processing of these alloys.

#### *3.4. Effect of Mo content on the hardness of the SPD-processed Ni alloys*

The measured hardness values of the cryorolled Low-Mo and High-Mo alloys were ~2650 and ~3730 MPa, respectively. Fig. 8 shows the hardness for the center, half-radius and periphery positions of the HPT-processed disks with low and high Mo contents. It is apparent that the hardness increases with both distance from the disk center and the number of turns of HPT. After 5 turns the hardness saturated for both alloy compositions and became homogeneous along the disk radii. The saturation values of hardness for the Low-Mo and High-Mo alloys were ~3200 and ~4300 MPa, respectively. This higher hardness for the larger Mo concentration is attributed to the higher dislocation density as discussed in more detail in the following section.

#### 4. Discussion

In the present study, cryorolling at LNT and HPT at RT were applied consecutively in order to refine the microstructure of two Ni alloys containing 0.3 and 5% Mo. The dislocation density after cryorolling was about one-half of the saturation value achieved by additional HPT as shown in Fig. 7. At the same time, the grain sizes of the cryorolled samples were at least one order of magnitude larger than the values determined after HPT. These observations demonstrate that for both compositions the increase of the dislocation density was faster than the refinement of the grain structure. Accordingly, the cryorolled samples had high dislocation density ( $15\text{-}35 \times 10^{14} \text{ m}^{-2}$ ) while the grain size remained relatively large ( $\sim 4 \mu\text{m}$ ). Despite this large grain size, the cryorolled alloys exhibited high hardness ( $\sim 2650$  and  $\sim 3730$  MPa for Low-Mo and High-Mo samples, respectively) due to the high dislocation density.

The rate of microstructure evolution during HPT is similar for both the 0.3 and 5% Mo alloys. At the half-radius and the periphery of the disk, the grain size, the HAGB fraction and the dislocation density achieve saturation values even after only  $\frac{1}{2}$  turn. In addition, in the disk center the grain size and the HAGB fraction saturate only after 20 turns due to the much

lower shear strain per turn. The dislocation density in the disk center reached a maximum value earlier after only 5 turns.

The results show the Mo concentration has a significant effect on the saturation values of the microstructural parameters. For 5% Mo, the grain size is about 30% smaller and the dislocation density is two times larger than for the 0.3% Mo alloy. This is due to the pinning effect of Mo on dislocations and grain boundaries which in practice hinders the occurrence of dynamic microstructural recovery during SPD. In addition, this effect also hinders the arrangement of dislocations into low energy configurations, such as dipoles, within the refined grains. As a consequence of this effect, the dislocation arrangement parameter,  $M$ , is much higher for the alloy containing the larger amount of Mo. At the same time, there was no major difference between the saturation values of the HAGB fractions for the Low-Mo and High-Mo samples, as their values were between 70 and 75%. This is similar to the HAGB fractions reported for Ni processed by HPT or a combination of ECAP and HPT [10]. Therefore, it appears that the higher Mo content has no significant effect on the saturation values of the HAGB and LAGB fractions. It should be noted, however, that EBSD investigations take into account only those LAGBs having misorientations between 2 and 15° and thus the LAGB fractions for misorientations lower than 2° may be different in these two alloys in accordance with the different values for the dislocation arrangement parameter  $M$ .

HPT processing of the cryorolled alloys led to significant hardening. The maximum hardness values achieved by a combination of cryorolling and HPT were ~3200 and ~4300 MPa for Low-Mo and High-Mo alloys, respectively. In order to study the strengthening mechanisms in the HPT-processed Ni alloys, the yield strength,  $\sigma_y$ , was estimated as one-third of the hardness and compared with the stress,  $\sigma_{Taylor}$ , calculated from the dislocation density,  $\rho$ , using the Taylor equation:

$$\sigma_{Taylor} = \sigma_0 + \alpha M^T G b \rho^{1/2}, \quad (2)$$

where  $\sigma_0$  is a threshold stress,  $\alpha$  is a constant describing the dislocation strengthening,  $G$  is the shear modulus ( $\sim 82$  GPa for Ni),  $b$  is the magnitude of the Burgers vector ( $\sim 0.25$  nm for Ni) and  $M^T$  is the Taylor factor. The alloys used in this investigation did not exhibit a strong texture and therefore  $M^T$  was taken as 3.06. The values of  $\sigma_0$  for the Low-Mo and High-Mo alloys were determined by uniaxial compression of samples annealed in a vacuum furnace at  $800^\circ\text{C}$  for 24 h and then quenched in oil to RT in order to retain the supersaturated solid solution state. The threshold stress values were obtained as  $\sim 40$  and  $\sim 180$  MPa for the Low-Mo and High-Mo alloys, respectively.

In eq. (2),  $\sigma_0$  includes the solid solution strengthening caused by the alloying elements in the Ni alloys and therefore the value of  $\sigma_0$  is much higher for the High-Mo alloy than for the Low-Mo material. In previous studies, eq. (2) was successfully applied for a calculation of the yield strength from the dislocation density for many SPD-processed metals and alloys without an additive Hall-Petch term [34]. In the present investigation, the dislocation density was determined by XLPA which measures both the statistically stored and the grain boundary dislocations. In SPD-processed microstructures, many dislocations are accumulated at the HAGBs through pile ups and therefore gliding dislocations interact with these dislocations rather than directly with the grain boundaries. As a consequence, HAGB hardening is practically included in eq. (2) and  $\alpha$  may be regarded as an effective dislocation strengthening parameter.

For the present Ni alloys, the values of the parameter  $\alpha$  in eq. (2) are not known initially since they are strongly influenced by the arrangements of the dislocations. Usually, the value of  $\alpha$  varies between 0.1 and 0.4 [37] and a less clustered dislocation structure is associated with a lower value of  $\alpha$  [38]. Therefore, the parameter  $\alpha$  in plastically deformed metals may depend on the types and concentrations of alloying elements, the stacking fault energy (SFE) and the applied strain. For example, it was shown that a lower SFE yields a

smaller  $\alpha$  since the clustering of highly dissociated dislocations is retarded by their difficult cross slip and climb [37]. For the present Low-Mo and High-Mo alloys processed by cryorolling and HPT, the value of  $\alpha$  was determined by minimizing the difference between the yield strength determined experimentally as one-third of the hardness ( $\sigma_Y$ ) and the strength values ( $\sigma_{Taylor}$ ) calculated from eq. (2). The significant difference between the dislocation arrangement parameters for the two alloys, as discussed in section 3.3, suggests that the value of  $\alpha$  may also differ for the Low-Mo and High-Mo materials. Thus, when the difference between the calculated and measured strength values is minimized by a least squares method, the values of  $\alpha$  for the Low-Mo and High-Mo alloys were refined independently. This fitting procedure yielded  $0.32 \pm 0.03$  and  $0.26 \pm 0.02$  for parameter  $\alpha$  for the Low-Mo and High-Mo alloys, respectively, where these values are similar to  $\alpha$  obtained previously for Ni processed by 6 passes of ECAP at RT ( $\sim 0.26$ ) [37]. The slightly lower value of  $\alpha$  for the High-Mo alloy is attributed to the less clustered dislocation structure after HPT in accordance with the higher dislocation arrangement parameter.

Fig. 9 plots the experimentally determined yield strength against the stress calculated from eq. (2) for the cryorolled and the HPT-processed Ni alloys using the refined values of  $\alpha$  of 0.32 and 0.26 for the Low-Mo and High-Mo alloys, respectively. Inspection of Fig. 9 shows that the measured and the calculated strength values agree within the experimental error. It is noted that the parameter  $\alpha$  may vary both with increasing distance from the center of the HPT disk and with the number of turns. Therefore, the values of  $\alpha$  were also calculated from eq. (2) for each position in the HPT disks using the condition  $\sigma_Y = \sigma_{Taylor}$ . No significant dependence was observed for  $\alpha$  in terms of the distance from the disk center or the numbers of turns. This demonstrates that the use of a single  $\alpha$  value for every strength value obtained for the same Mo content is a good approximation in determining  $\alpha$ .

## 5. Summary and conclusions

1. Ni alloys with low (0.3%) and high (5%) Mo contents were subjected to cryorolling and subsequent HPT at RT. The results show both alloys remain in a solid solution state even after cryorolling and HPT. As the equilibrium solubility limit of Mo in Ni is 0.6%, the alloy with 5% Mo is a supersaturated solid solution.

2. Although the grain size was not refined into the UFG regime during cryorolling, there were very high dislocation densities ( $\sim 15\text{-}35 \times 10^{14} \text{ m}^{-2}$ ) in both alloys. HPT at RT led to a further enhancement in the dislocation density up to  $\sim 30\text{-}60 \times 10^{14} \text{ m}^{-2}$  and a concomitant gradual grain refinement below 200 nm. Irrespective of the Mo content, the saturation of the dislocation density occurred earlier than for the grain size during combined cryorolling and HPT. A homogeneous spatial distribution of the grain size along the HPT disk radius was achieved only after 20 turns whereas the dislocation density became homogeneous even after 5 turns.

3. The minimum grain size and maximum dislocation density achieved by HPT in the alloy with 0.3% Mo was  $\sim 180 \text{ nm}$  and  $\sim 30 \times 10^{14} \text{ m}^{-2}$ , respectively. For the higher Mo content (5%), the saturation grain size was  $\sim 125 \text{ nm}$  and the dislocation density was  $\sim 60 \times 10^{14} \text{ m}^{-2}$ . These values are respectively smaller and higher than in the 0.3% Mo alloy due to the pinning effect of Mo atoms on the lattice defects. This effect also hinders the clustering of dislocations within the grains as indicated by the higher value of the dislocation arrangement parameter.

4. The hardness for both alloys saturated and became homogeneous along the disk radii after 5 turns of HPT. The maximum hardness values achieved for 0.3% and 5% Mo concentrations were  $\sim 3200$  and  $\sim 4300 \text{ MPa}$ , respectively. The higher saturation hardness with 5% Mo is in accordance with the microstructural observations. It is demonstrated that the hardening caused by the combined process of cryorolling and HPT may be related to the increase of the dislocation density using the Taylor equation. The  $\alpha$  parameter in this equation has a lower value for the higher Mo content due to the less clustered dislocation structure.

**Acknowledgements**

This work was supported by the Hungarian Scientific Research Fund, OTKA, Grant no. K-109021. The authors are grateful to Mr. Alajos Ö. Kovács and Mr. Gábor Varga for the DSC and EBSD investigations, respectively. Two of the authors were supported by the European Research Council under ERC Grant Agreement No. 267464-SPDMETALS (YH and TGL).

Accepted manuscript

**References**

1. R.Z. Valiev, I. Sabirov, A.P. Zhilyaev, T.G. Langdon, Bulk nanostructured metals for innovative applications, *JOM* 64 (2012) 1134–1142.
2. R.Z. Valiev, A.P. Zhilyaev, T.G. Langdon, *Bulk Nanostructured Materials: Fundamentals and Applications*, John Wiley & Sons, Inc., Hoboken, NJ, 2014.
3. R.Z. Valiev, Y. Estrin, Z. Horita, T. G. Langdon, M.J. Zehetbauer, Y. Zhu, Producing bulk ultrafine-grained materials by severe plastic deformation, *JOM* 68 (2016) 1216–1226.
4. A.P. Zhilyaev, G.V. Nurislamova, B.K. Kim, M.D. Baro, J.A. Szpunar, T.G. Langdon, Experimental parameters influencing grain refinement and microstructural evolution during high-pressure torsion, *Acta Mater.* 51 (2003) 753–765.
5. A.P. Zhilyaev, T.G. Langdon, Using high-pressure torsion for metal processing: Fundamentals and applications, *Prog. Mater. Sci.* 53 (2008) 893-979.
6. A. Hohenwarter, A. Bachmaier, B. Gludovatz, S. Scheriau, R. Pippan, Technical parameters affecting grain refinement by high pressure torsion, *Int. J. Mater. Res.* 100 (2009) 1653-1661.
7. Y.B. Wang, J.C. Ho, Y. Cao, X.Z. Liao, H.Q. Li, Y.H. Zhao, E.J. Lavernia, S.P. Ringer, Y.T. Zhu, Dislocation density evolution during high pressure torsion of a nanocrystalline Ni-Fe alloy, *Appl. Phys. Lett.* 94 (2009) Article ID 091911.
8. M. Kawasaki, Different models of hardness evolution in ultrafine-grained materials processed by high-pressure torsion, *J. Mater. Sci.* 49 (2014) 18-34.
9. J. Gubicza, *Defect Structure in Nanomaterials*, Woodhead Publishing, Cambridge, UK, 2012.

10. A.P. Zhilyaev, B.K. Kim, J.A. Szpunar, M.D. Baro, T.G. Langdon, The microstructural characteristics of ultrafine-grained nickel, *Mater. Sci. Eng. A* 391 (2005) 377–389.
11. A.P. Zhilyaev, J. Gubicza, G.V. Nurislamova, A. Révész, S. Surinach, M.D. Baro, T. Ungár, Microstructural characterization of ultrafine-grained nickel, *Phys Status Solidi (a)* 198 (2003) 263–271.
12. S. Sabbaghianrad, T.G. Langdon, A critical evaluation of the processing of an aluminum 7075 alloy using a combination of ECAP and HPT, *Mater. Sci. Eng. A* 596 (2014) 52–58.
13. T.R. Lee, C.P. Chang, P.W. Kao, The tensile behavior and deformation microstructure of cryorolled and annealed pure nickel, *Mater. Sci. Eng. A* 408 (2005) 131–135.
14. J. Gubicza, N.Q. Chinh, Z. Horita, T.G. Langdon, Effect of Mg addition on microstructure and mechanical properties of aluminum, *Mater. Sci. Eng. A* 387–389 (2004) 55–59.
15. L. Balogh, T. Ungár, Y. Zhao, Y.T. Zhu, Z. Horita, C. Xu, T.G. Langdon, Influence of stacking-fault energy on microstructural characteristics of ultrafine-grain copper and copper-zinc alloys, *Acta Mater.* 56 (2008) 809–820.
16. J. Gubicza, I. Schiller, N.Q. Chinh, J. Illy, Z. Horita, T.G. Langdon, The effect of severe plastic deformation on precipitation in supersaturated Al-Zn-Mg alloys, *Mater. Sci. Eng. A* 460–461 (2007) 77–85.
17. S. Qu, X.H. An, H.J. Yang, C.X. Huang, G. Yang, Q.S. Zang, Z.G. Wang, S.D. Wu, Z.F. Zhang, Microstructural evolution and mechanical properties of Cu–Al alloys subjected to equal channel angular pressing, *Acta Mater.* 57 (2009) 1586–1601.

18. P.V. Liddicoat, X.Z. Liao, Y. Zhao, Y. Zhu, M.Y. Murashkin, E.J. Lavernia, R.Z. Valiev, S.P. Ringer, Nanostructural hierarchy increases the strength of aluminium alloys, *Nature Comm.* 1 (2010) Art. No. 63.
19. M. Dopita, M. Janecek, R. Kuzel, H.J. Seifert, S. Dobatkin, Microstructure evolution of CuZr polycrystals processed by high-pressure torsion, *J. Mater. Sci.* 45 (2010) 4631–4644.
20. R. Kuzel, M. Janecek, Z. Matej, J. Cizek, M. Dopita, O. Srba, Microstructure of Equal-Channel Angular Pressed Cu and Cu-Zr Samples Studied by Different Methods, *Metall. Mater. Trans. A* 41 (2010) 1174–1190.
21. A. Alhamidi, K. Edalati, Z. Horita, S. Hirosawa, K. Matsuda, D. Terada, Softening by severe plastic deformation and hardening by annealing of aluminum–zinc alloy: Significance of elemental and spinodal decompositions, *Mater. Sci. Eng. A* 610 (2014) 17–27.
22. O. Andreau, J. Gubicza, N.X. Zhang, Y. Huang, P. Jenei, T.G. Langdon, Effect of short-term annealing on the microstructures and flow properties of an Al-1% Mg alloy processed by high-pressure torsion, *Mater. Sci. Eng. A* 615 (2014) 231-239.
23. S.V. Dobatkin, J. Gubicza, D.V. Shangina, N.R. Bochvar, N.U. Tabachkov, High strength and good electrical conductivity in Cu-Cr alloys processed by severe plastic deformation, *Mater. Lett.* 153 (2015) 5-9.
24. D.E. Brown, M.N. Mahmood, M.C.M. Man, A.K. Turner, Preparation and characterization of low overvoltage transition metal alloy electrocatalysts for hydrogen evolution in alkaline solutions, *Electrochim. Acta* 29 (1984) 1551-1556.
25. R. Schulz, J.Y. Huot, M.L. Trudeau, L. Dignard-Bailey, Z.H. Yan, S. Jin, A. Lamarre, E. Ghali, A.V. Neste, Nanocrystalline Ni-Mo alloys and their application in electrocatalysis, *J. Mater. Res.* 9 (1994) 2998–3008.

26. J.R. McKone, B.F. Sadler, C.A. Werlang, N.S. Lewis, H.B. Gray, Ni–Mo Nanopowders for Efficient Electrochemical Hydrogen Evolution, *ACS Catal.* 3 (2013) 166–169.
27. P.P. Bhattacharjee, R.K. Ray, A. Upadhyaya, Nickel base substrate tapes for coated superconductor applications, *J. Mater. Sci.* 42 (2007) 1984–2001.
28. T. Ohgai, Y. Tanaka, R. Washio, Nanocrystalline structure and soft magnetic properties of nickel–molybdenum alloy thin films electrodeposited from acidic and alkaline aqueous solutions, *J. Solid State Electrochem.* 17 (2013) 743–750.
29. E. Beltowska-Lehman, A. Bigos, P. Indyka, M. Kot, Electrodeposition and characterization of nanocrystalline Ni-Mo coatings, *Surf. Coat. Tech.* 211 (2011) 67-71.
30. R.B. Figueiredo, P.R. Cetlin, T.G. Langdon, Using finite element modeling to examine the flow processes in quasi-constrained high-pressure torsion, *Mater. Sci. Eng. A* 528 (2011) 8198-8204.
31. L.S. Tóth, B. Beausir, C.F. Gu, Y. Estrin, N. Scheerbaum, C.H.J. Davies, Effect of grain refinement by severe plastic deformation on the next-neighbor misorientation distribution, *Acta Mater.* 58 (2010) 6706-6716.
32. L.S. Tóth, C. Gu, Ultrafine-grain metals by severe plastic deformation, *Mater. Charact.* 92 (2014) 1-14.
33. J. Nelson, D. Riley, An experimental investigation of extrapolation methods in the derivation of accurate unit-cell dimensions of crystals, *Proc. Phys. Soc. Lond.* 57 (1945) 160–177.
34. G. Ribárik, J. Gubicza, T. Ungár, Correlation between strength and microstructure of ball-milled Al–Mg alloys determined by X-ray diffraction, *Mater. Sci. Eng. A* 387–389 (2004) 343–347.

35. Y. Mishima, S. Ochiai, T. Suzuki, Lattice parameters of Ni( $\gamma$ ), Ni<sub>3</sub>Al( $\gamma'$ ) and Ni<sub>3</sub>Ga( $\gamma'$ ) solid solutions with additions of transition and B-subgroup elements, *Acta Metal.* 33 (1985) 1161-1169.
36. J. Gubicza, *X-ray Line Profile Analysis in Materials Science*, IGI-Global, Hershey, PA, USA, 2014.
37. J. Gubicza, N. Q. Chinh, J.L. Lábár, S. Dobatkin, Z. Hegedűs, T. G. Langdon, Correlation between microstructure and mechanical properties of severely deformed metals, *J. Alloys Compd.* 483 (2009) 271-274.
38. F. Hernandez Olivares, J. Gil Sevillano, A quantitative assessment of forest-hardening in FCC metals, *Acta Metall.* 35(1987) 631-641.

**Figure and table captions**

Figure 1: EBSD images for the cryorolled Low-Mo (a and b) and High-Mo (c and d) Ni alloys. The HAGBs are indicated by black lines.

Figure 2: EBSD images for the Low-Mo alloy processed by HPT: center (a) and periphery (b) for 1/2 turn, and center (c) and periphery (d) for 20 revolutions.

Figure 3: EBSD images for the High-Mo alloy processed by HPT: center (a) and periphery (b) for 1/2 turn, and center (c) and periphery (d) for 20 revolutions.

Figure 4: The grain size in the center, half-radius and periphery for the Low-Mo (a) and High-Mo (b) disks processed by different turns of HPT. The scales of the vertical axes in the two images are the same for an easier comparison of the different grain size values in the Low-Mo and High-Mo alloys.

Figure 5: HAGB fraction in the center, half-radius and periphery for the Low-Mo (a) and High-Mo (b) disks processed by different turns of HPT. The HAGB fractions for the cryorolled alloys are also indicated by the horizontal lines.

Figure 6: CMWP fitting of the X-ray diffraction pattern taken in the center of the High-Mo alloy disk processed by 20 turns of HPT. The open circles and the solid line represent the measured data and the fitted curve, respectively. The intensity is in logarithmic scale. The inset shows a magnified part of the diffractogram in linear intensity scale where the difference between the measured and the fitted patterns is also given at the bottom of the image.

Figure 7: The dislocation density in the center, half-radius and periphery for the Low-Mo (a) and High-Mo (b) disks processed by different turns of HPT. The scales of the vertical axes in the two images are the same for an easier comparison of the very different dislocation density values in the Low-Mo and High-Mo alloys. The dislocation densities for the cryorolled alloys are also indicated by the horizontal lines.

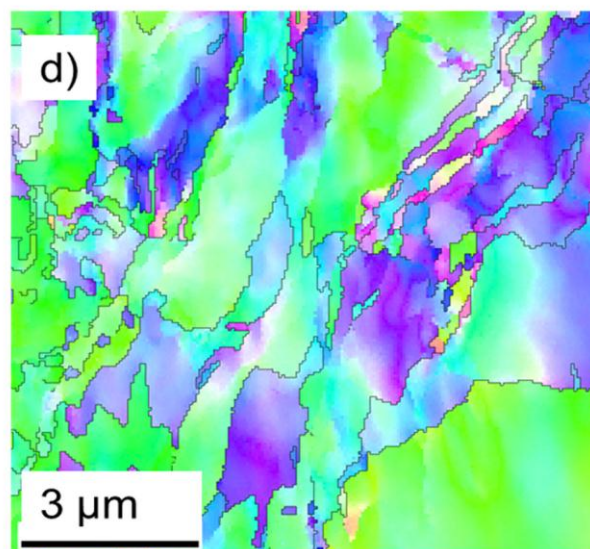
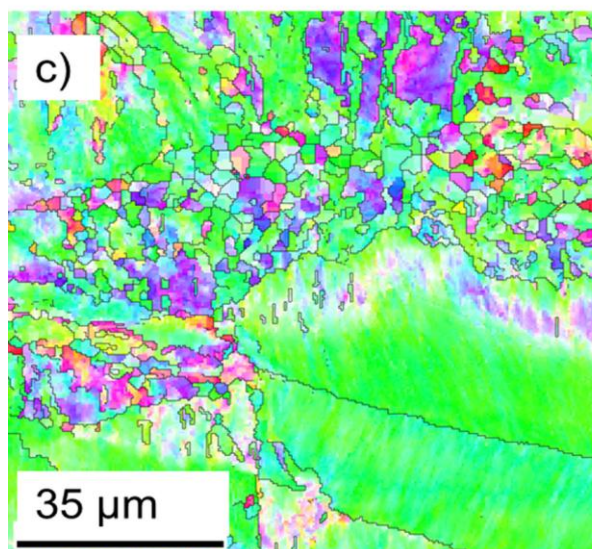
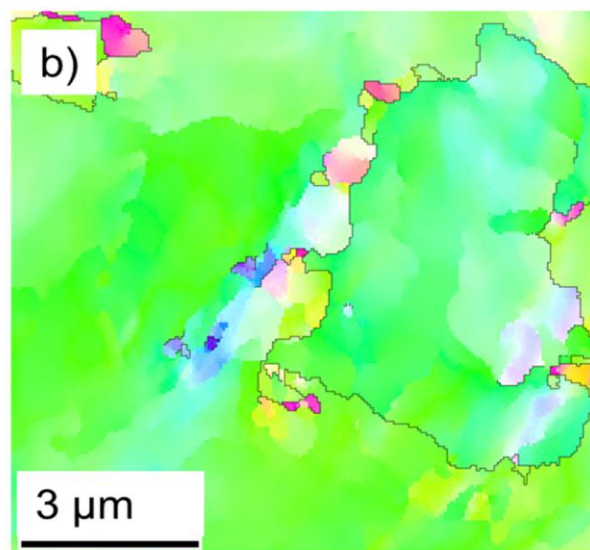
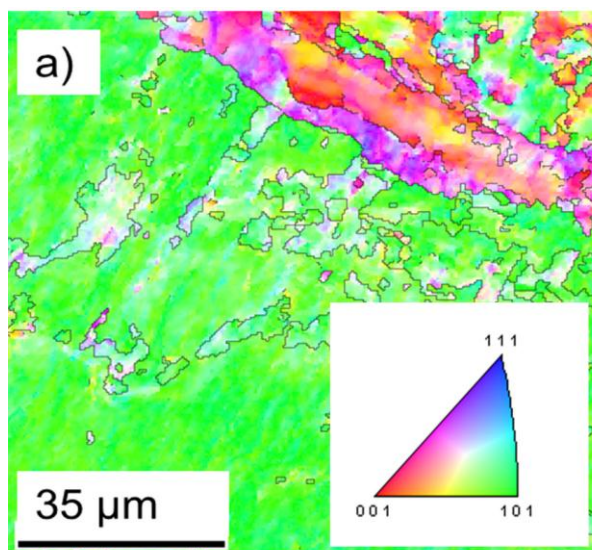
Figure 8: The hardness in the center, half-radius and periphery for the Low-Mo (a) and High-Mo (b) disks processed by different turns of HPT. The scales of the vertical axes in the two images are the same for an easier comparison of the very different hardness values in the Low-Mo and High-Mo alloys. The hardness values for the cryorolled alloys are also indicated by the horizontal lines.

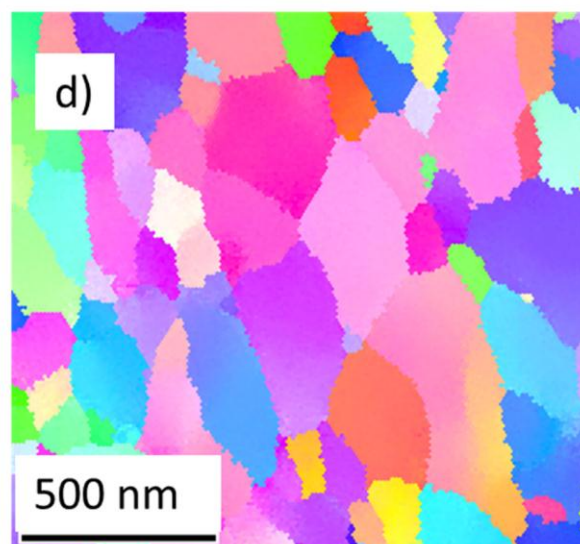
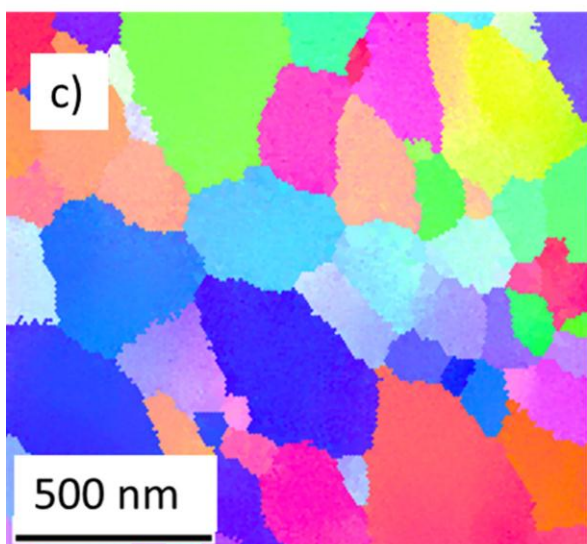
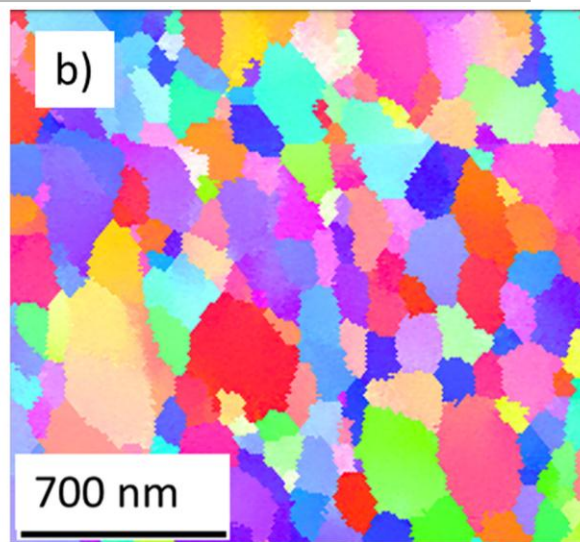
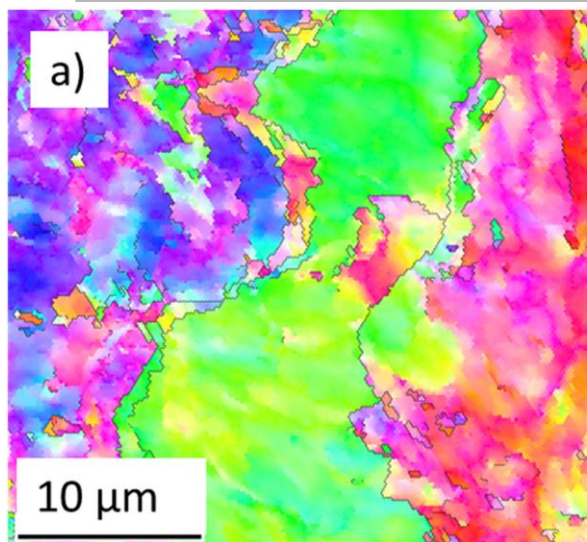
Figure 9: The experimentally determined yield strength ( $\sigma_Y$ ) versus the stress calculated from the Taylor equation ( $\sigma_{Taylor}$ ) for the cryorolled Low-Mo and High-Mo alloys, and the HPT processed disks at the center, half-radius and periphery for  $\frac{1}{2}$ , 5 and 20 turns. The Taylor stress was calculated using 0.32 and 0.26 as  $\alpha$  for the Low-Mo and High-Mo alloys, respectively.

Table 1: Chemical composition of the alloys with low and high Mo contents as determined by EDS.

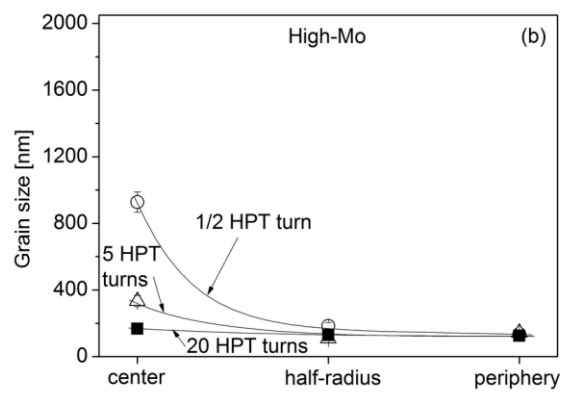
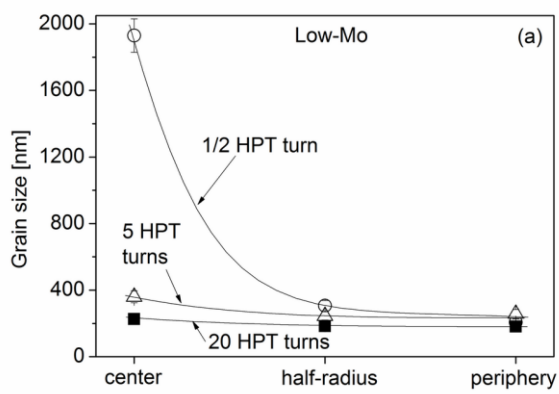
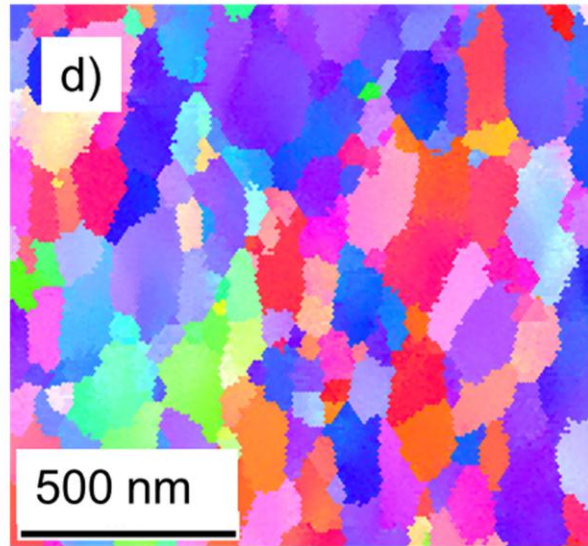
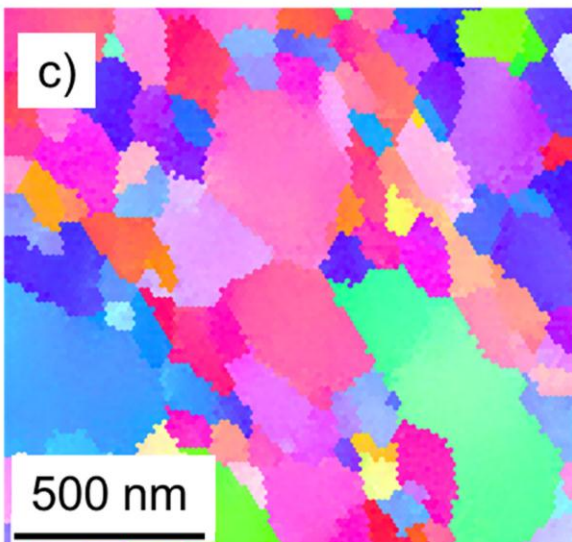
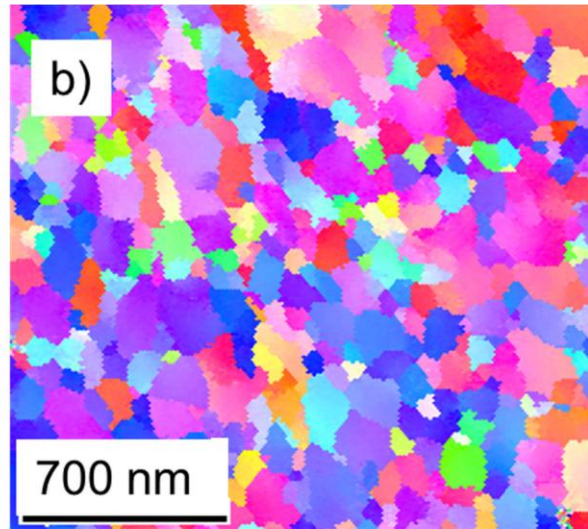
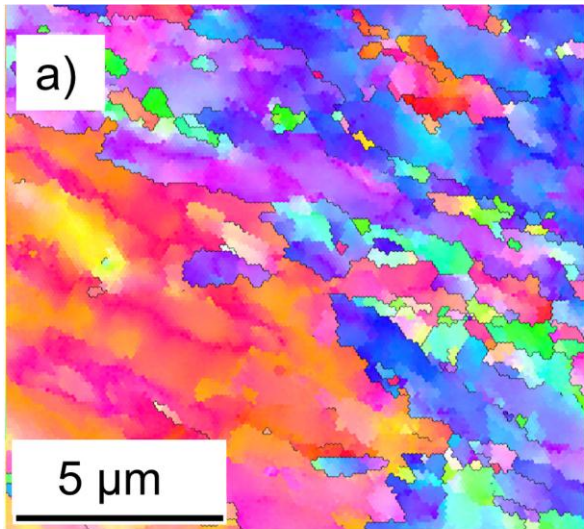
**Table 1:** Chemical composition of the alloys with low and high Mo contents as determined by EDS.

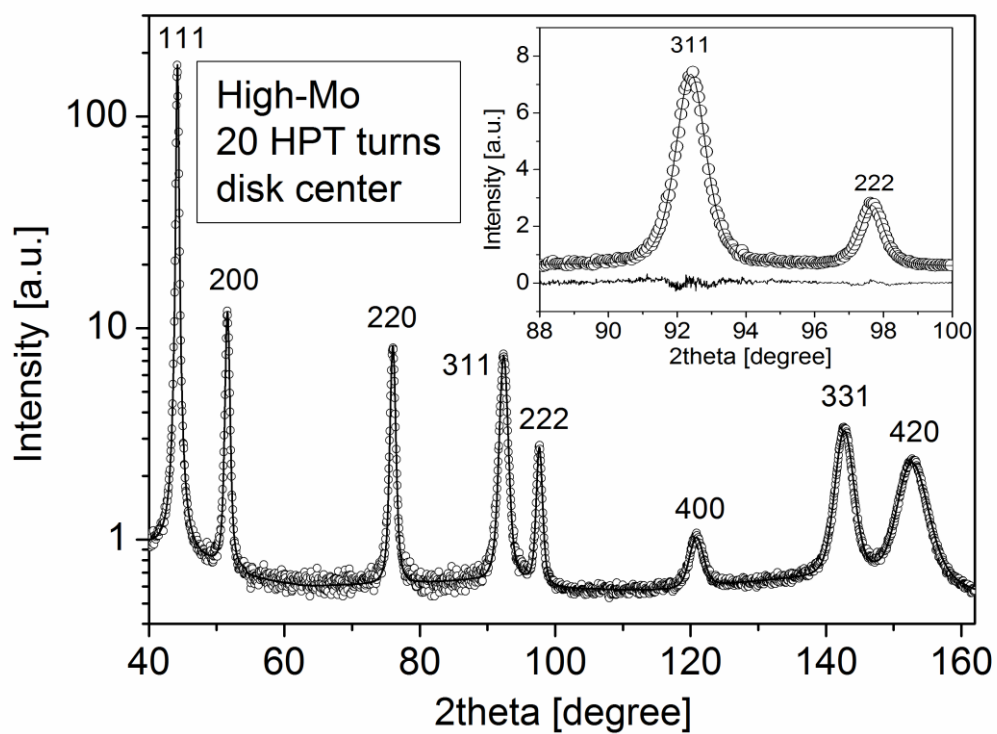
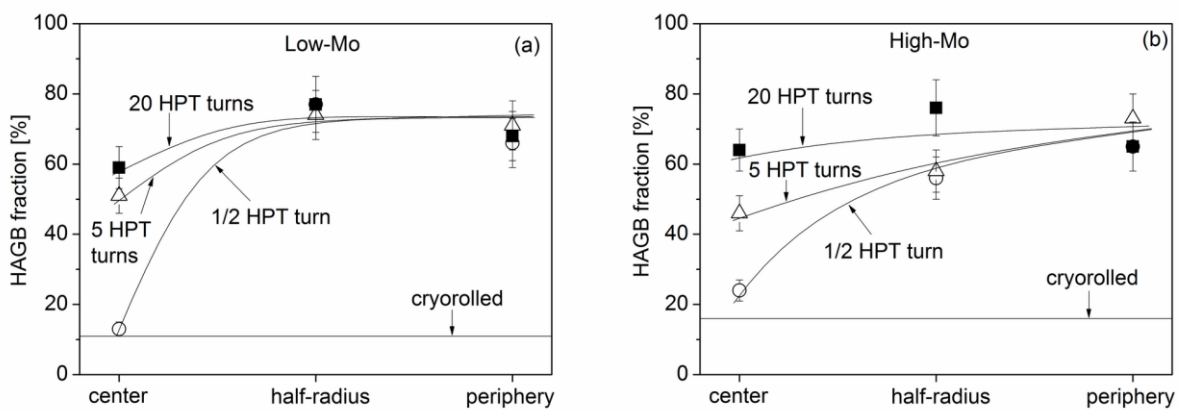
Low-Mo alloy					
Element	Ni	Mo	Al	Si	Fe
At%	98.29	0.28	0.84	0.34	0.25
High-Mo alloy					
Element	Ni	Mo	Al	Si	Fe
At%	93.70	5.04	1.08	0.05	0.13

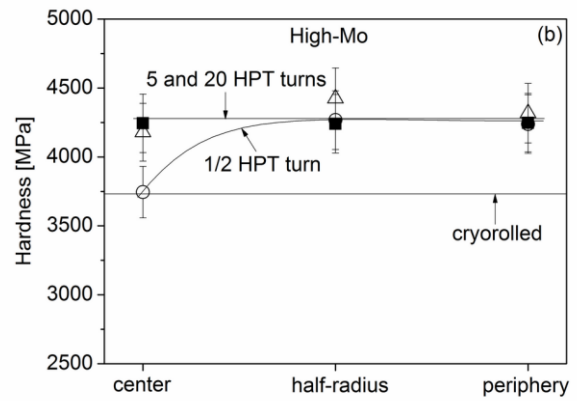
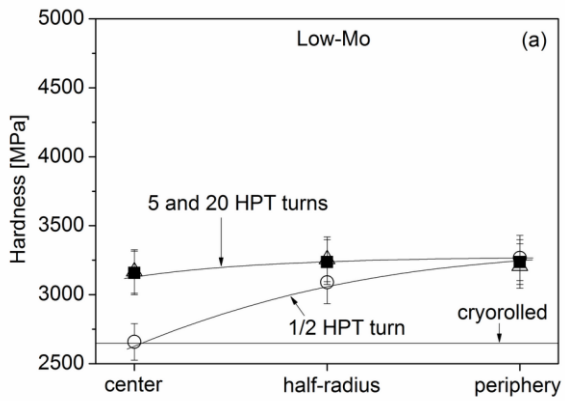
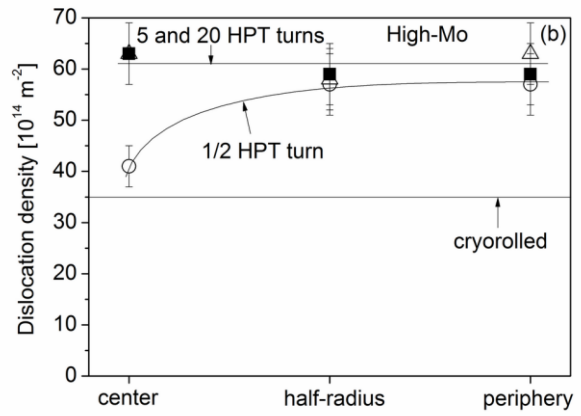
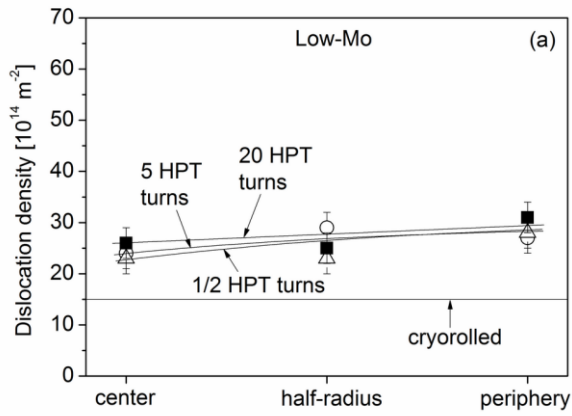


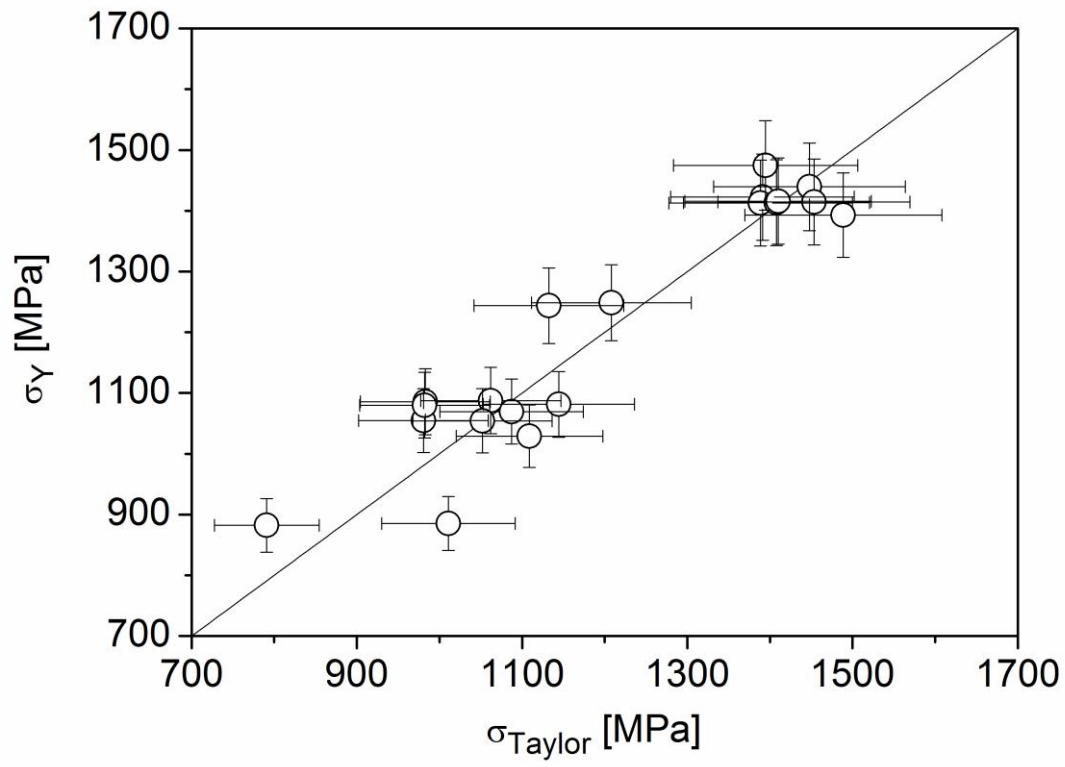


Accepted









Accepted manu